High order finite point method for the solution to the sound propagation problems

Jaroslav Bajko*, Libor Čermák, Miroslav Jícha

Faculty of Mechanical Engineering, Brno University of Technology, Technická 2896/2, 616 69 Brno, Czech Republic

Highlights

- The accuracy of the meshfree Finite point method (FPM) was improved.
- The Godunov Riemann solver was used with the polynomial reconstruction.
- Modified FPM was used to solve the acoustic propagation problems.
- The propagation of sound was simulated using the linearized Euler equations.
- High order of the FPM was confirmed by the convergence study.

Abstract

In this paper we present an accuracy improvement of the meshfree Finite point method. This high-order method has been used to solve the sound propagation problems, which can be modelled by linearized Euler equations. High accuracy has been obtained using polynomial reconstruction of variables involved in the Riemann solver. The order of the meshfree method will be verified on 2D acoustic pulse problem which serves as a benchmark problem with known analytical solution.
© 2014 Elsevier B.V. All rights reserved.

1. Introduction

Computational aeroacoustics (CAA) becomes an important research field with the permanent increase of computer performance and accessible memory. The main challenge in CAA is the computation of noise generation and propagation problems using various numerical techniques. One of the possible options is a direct computation from governing partial differential equations (PDEs), but only provided that the underlying numerical methods reach

---

* Corresponding author. Tel.: +420 774597481.
 E-mail addresses: jarobaj@email.cz, y115413@stud.fme.vutbr.cz (J. Bajko).

high spatial and time accuracy. The reason for this strict requirement is the aerodynamic and acoustic disparity, cf. [1].

The standard solution to the CAA problems is based on numerical methods, which require a fixed mesh or grid, such as finite difference methods [2], finite volume methods [3–5] or finite element methods and their variations [6,7]. An alternative approach represent numerical methods known as meshfree or meshless methods, cf. [8–10], which do not require a predefined mesh. A frequently mentioned advantage of meshfree methods in comparison to the standard mesh-based methods is the absence of time consuming mesh generation. Another, even more important, advantage is their high accuracy. On the other hand, these benefits are offset by additional computational costs. Li, et al., [11] and Wang [12] have recently proposed a meshfree method for CAA based on a radial basis function interpolation. Antunes, cf. [13] has developed a meshfree modification of the method of fundamental solutions.

We have studied the properties of meshfree Finite point method (FPM) proposed by E. Oñate [14–19] to solve the linearized Euler equations (LEE). This hyperbolic system of equations can be seen as a model of sound propagation, cf. [20,21]. We have improved the accuracy of FPM using the polynomial reconstruction of variables in the Riemann solver, [3–5]. A benchmark 2D acoustic pulse problem, proposed by Tam and Webb [2] has been solved using high order FPM. The order of the proposed method has been estimated using a convergence study.

2. Outline

The first part of this paper is devoted to the derivation of 2D LEE. A section describing the FPM in detail follows immediately. An approximation of variables in FPM is performed locally using weighted least squares (WLSQ) method, cf. Section 4.2. The governing PDEs are then collocated at each point in the domain of interest leading to a system of ordinary differential equations (ODEs). A necessary step after semi-discretization is the stabilization of the numerical scheme with respect to the hyperbolic nature of the governing LEE. The accuracy of FPM is strongly related to the accuracy of the directional flux between two neighbouring points. Godunov's method is one of the approximation techniques, that makes it possible to obtain the directional flux by solving the Riemann problem, cf. Section 4.7. By using the more accurate initial condition for the Riemann problem (left and right states), the more accurate solution of the governing equations is obtained. Therefore, a polynomial reconstruction of the left and right states, cf. Section 4.8, is proposed.

The second important part of the paper is devoted to the numerical experiments. A solution to the 2D acoustic pulse problem using high order FPM is presented, cf. Section 5.1. We compare the analytical and numerical solutions computed using different polynomial reconstructions and different space discretizations of the domain of interest, resulting to a convergence study in Section 5.5. A solution to the 2D wall bounded acoustic pulse problem on rectangular and circular geometry is presented in Sections 5.6–5.11.

3. 2D linearized Euler equations

Let us denote the vector function $\mathbf{w}(\mathbf{x}, t) := (\rho(\mathbf{x}, t), u(\mathbf{x}, t), v(\mathbf{x}, t), p(\mathbf{x}, t))^T$ with primitive (physical) variables, i.e. the density, velocity components and pressure, respectively. Therefore, the compressible 2D Euler equations in matrix form read as

$$\frac{\partial \mathbf{w}}{\partial t} + \mathbb{A}_1(\mathbf{w})\frac{\partial \mathbf{w}}{\partial x} + \mathbb{A}_2(\mathbf{w})\frac{\partial \mathbf{w}}{\partial y} = \mathbf{0}, \quad \mathbf{x} = (x, y) \in \mathbb{R}^2, \ t > 0, \tag{1}$$

where the Jacobian matrices of this hyperbolic system are given as follows

$$\mathbb{A}_1(\mathbf{w}) = \begin{pmatrix} u & \rho & 0 & 0 \\ 0 & u & 0 & 1/\rho \\ 0 & 0 & u & 0 \\ 0 & \gamma p & 0 & u \end{pmatrix}, \qquad \mathbb{A}_2(\mathbf{w}) = \begin{pmatrix} v & 0 & \rho & 0 \\ 0 & v & 0 & 0 \\ 0 & 0 & v & 1/\rho \\ 0 & 0 & \gamma p & v \end{pmatrix}, \tag{2}$$

where γ is the adiabatic index ($\gamma = 1.4$ for diatomic gases). The quantities included in $\mathbf{w}$ can be decomposed into a *reference state* (or *mean value*) $\mathbf{w}_0(\mathbf{x})$ and a time dependent *fluctuating* (or *perturbation*) part $\mathbf{w}'(\mathbf{x}, t)$, cf. [1,20,21] in

the following way

$$\mathbf{w} = \begin{pmatrix} \rho \\ u \\ v \\ p \end{pmatrix} = \underbrace{\begin{pmatrix} \rho_0 \\ u_0 \\ v_0 \\ p_0 \end{pmatrix}}_{\mathbf{w}_0} + \underbrace{\begin{pmatrix} \rho' \\ u' \\ v' \\ p' \end{pmatrix}}_{\mathbf{w}'}, \quad \mathbf{x} = (x, y) \in \mathbb{R}^2, \ t > 0. \tag{3}$$

Assuming that the fluctuating variables $\mathbf{w}'$ are negligible in comparison to the reference states $\mathbf{w}_0$, i.e.

$$|\rho'| \ll |\rho_0|, \qquad |u'| \ll \|\mathbf{u}_0\|, \qquad |v'| \ll \|\mathbf{u}_0\|, \qquad |p'| \ll |p_0|, \tag{4}$$

where $\mathbf{u}_0 = (u_0, v_0)^T$, the Jacobian matrices $\mathbb{A}_j(\mathbf{w})$ can be approximated as follows

$$\mathbb{A}_j(\mathbf{w}_0 + \mathbf{w}') \approx \mathbb{A}_j(\mathbf{w}_0), \quad j = 1, 2. \tag{5}$$

Substituting $\mathbf{w} = \mathbf{w}_0 + \mathbf{w}'$ into (1) and arranging the equations with respect to the unknown fluctuating variables $\mathbf{w}'$, the 2D linearized Euler equations in matrix form read as

$$\frac{\partial \mathbf{w}'}{\partial t} + \mathbb{A}_1(\mathbf{w}_0) \frac{\partial \mathbf{w}'}{\partial x} + \mathbb{A}_2(\mathbf{w}_0) \frac{\partial \mathbf{w}'}{\partial y} + \mathbf{H} = \mathbf{0}, \tag{6}$$

where $\mathbb{A}_1(\mathbf{w}_0)$, $\mathbb{A}_2(\mathbf{w}_0)$ are linearized Jacobian matrices and $\mathbf{H}$ is the vector containing the derivatives of the mean flow

$$\mathbf{H} = \mathbb{A}_1(\mathbf{w}_0) \frac{\partial \mathbf{w}_0}{\partial x} + \mathbb{A}_2(\mathbf{w}_0) \frac{\partial \mathbf{w}_0}{\partial y}. \tag{7}$$

4. Finite point method

The meshfree Finite point method has been presented by Oñate et al., [14] to solve the fluid flow problems. Other improvements of this method and successful solution to the compressible Euler equations have been published by Ortega et al., [18,19,22] and other authors [23–25]. Let us summarize the derivation of FPM.

4.1. Basic notation

Definition 4.1. Let $\Omega \subset \mathbb{R}^d$ ($d = 1$, 2 or 3 in practise) be the domain and Γ its boundary. We define the *global cloud* $\hat{\Omega}$ as a finite set of points from $\overline{\Omega}$ which discretizes the closed domain $\overline{\Omega}$. We write

$$\hat{\Omega} = \{\mathbf{x}_i\}_{i=1}^n. \tag{8}$$

The *ith local cloud* $\hat{\Omega}_i$ we define as a finite set

$$\hat{\Omega}_i = \hat{\Omega} \cap \Omega_i \tag{9}$$

where $\Omega_i = \left\{\mathbf{x} \in \mathbb{R}^d, \|\mathbf{x} - \mathbf{x}_i\| < r_i\right\}$ is an open ball and the union of Ω_i creates the covering of $\overline{\Omega}$, i.e. $\overline{\Omega} \subseteq \bigcup_{i=1}^n \Omega_i$. Similarly we write

$$\hat{\Omega}_i = \left\{\mathbf{x}_j^i\right\}_{j=1}^{n_i}, \tag{10}$$

where n_i is the number of points in the local cloud $\hat{\Omega}_i$. Moreover, the particular point $\mathbf{x}_i = \mathbf{x}_1^i$ is called the *star point*[1] of the local cloud $\hat{\Omega}_i$.

---

[1] Star points $\mathbf{x}_i$ according to (9) are centres of open balls Ω_i. For the sake of lucidity, the star point will be always written as the first point in explicit notation of a local cloud $\hat{\Omega}_i$.

Discretization of a domain by particular global cloud and one local cloud with its star point is illustrated in Fig. 1.
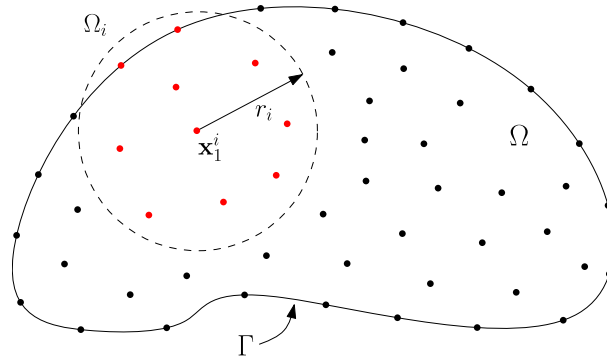

Fig. 1. Domain Ω with boundary Γ, one particular domain Ω_i (open ball), star point $\mathbf{x}_1^i$, global cloud (black and red dots), local cloud corresponding to $\mathbf{x}_1^i$ (red dots). (For interpretation of the references to colour in this figure legend, the reader is referred to the web version of this article.)

4.2. Local approximation using WLSQ method

Consider a closed domain $\overline{\Omega}$ covered by n domains Ω_i and let $\hat{\Omega}_i = \left\{ \mathbf{x}_j^i \right\}_{j=1}^{n_i}$ denotes the corresponding ith local cloud. We wish to find the local approximation $\hat{w}_i : \Omega_i \to \mathbb{R}$ for the local cloud $\hat{\Omega}_i$ in the form

$$\hat{w}_i(\mathbf{x}) = \sum_{l=1}^{m} \alpha_l^i p_l(\mathbf{x}) = \mathbf{p}^T(\mathbf{x})\boldsymbol{\alpha}_i, \quad i = 1, \ldots, n, \tag{11}$$

where

$$\boldsymbol{\alpha}_i = \left(\alpha_1^i, \alpha_2^i, \ldots, \alpha_m^i \right)^T \in \mathbb{R}^m \tag{12}$$

$$\mathbf{p}^T(\mathbf{x}) = \left(p_1(\mathbf{x}), p_2(\mathbf{x}), \ldots, p_m(\mathbf{x}) \right). \tag{13}$$

Functions $p_l : \mathbb{R}^d \to \mathbb{R}$, $l = 1, \ldots, m$, form a basis $\mathcal{B}$ of a function space $\mathcal{F}$. We assume that the basis $\mathcal{B}$ always contains a constant function, e.g. $1 \in \mathcal{B}$. The *complete polynomial basis of degree ν* is often proposed, cf. [10,19]. For $d = 2$ and $\nu = 2$, it can be used e.g.

$$\mathcal{B} = \left\{ 1, x, y, x^2, xy, y^2 \right\}. \tag{14}$$

For $d = 2$ and $\nu = 3$, e.g.

$$\mathcal{B} = \left\{ 1, x, y, x^2, xy, y^2, x^3, x^2y, xy^2, y^3 \right\}. \tag{15}$$

Proposition 4.1. *Let $\hat{\Omega}_i = \left\{ \mathbf{x}_j^i \right\}_{j=1}^{n_i}$ denotes the ith local cloud and $\mathbf{w}_i = \left(w_1^i, w_2^i, \ldots, w_{n_i}^i \right)^T$ is the vector of function values prescribed at local cloud points $\mathbf{x}_j^i$. Moreover let the function basis $\mathcal{B} = \{ p_l(\mathbf{x}); \ l = 1, 2, \ldots, m \}$ is selected. Then the coefficients $\boldsymbol{\alpha}_i$ of the linear combination* (11) *can be obtained in the weighted least squares sense as*

$$\boldsymbol{\alpha}_i = \mathbf{C}_i \mathbf{w}_i, \tag{16}$$

where

$$\mathbf{C}_i := \mathbf{A}_i^{-1} \mathbf{B}_i, \quad \mathbf{A}_i := \mathbf{P}_i^T \boldsymbol{\Phi}_i \mathbf{P}_i \quad and \quad \mathbf{B}_i := \mathbf{P}_i^T \boldsymbol{\Phi}_i \tag{17}$$

are matrices of type $(m \times n_i)$, $(m \times m)$ and $(m \times n_i)$, respectively. Matrix $\mathbf{P}_i$ of type $(n_i \times m)$ and diagonal matrix Φ_i of order n_i are constructed as follows

$$\mathbf{P}_i := \begin{pmatrix} \mathbf{p}^T(\mathbf{x}_1^i) \\ \mathbf{p}^T(\mathbf{x}_2^i) \\ \vdots \\ \mathbf{p}^T(\mathbf{x}_{n_i}^i) \end{pmatrix}, \qquad \Phi_i := \mathrm{diag}\left\{ \phi_i(\mathbf{x}_j^i) \right\}_{j=1}^{n_i}, \tag{18}$$

where $\phi_i : \mathbb{R}^d \to \mathbb{R}$ denotes a weighting function associated with the star point $\mathbf{x}_1^i$, cf. [19].

We suppose that the number of points n_i in $\hat{\Omega}_i$ always equals or is greater than the number of basis functions m, i.e. always holds $n_i \geq m$. In the case of equality $n_i = m$, then the coefficients $\boldsymbol{\alpha}_i$ are uniquely determined by enforcing $\hat{w}_i(\mathbf{x})$ to pass through the prescribed values $\mathbf{w}_i$ at points $\mathbf{x}_j^i$. Thus, the function $\hat{w}_i(\mathbf{x})$ interpolates values $\mathbf{w}_i$ at local cloud points. More desired approximation in WLSQ sense occurs when the inequality $n_i > m$ holds.

4.3. Weighting function

Weighting function $\phi_i(\mathbf{x})$ is the Gaussian-like function, cf. [18,19], given by three parameters (ω, k, γ). Values at $\mathbf{x} = \mathbf{x}_j^i$ are computed as

$$\phi_i(\mathbf{x}_j^i) = \frac{\exp(-\left(d_j/\bar{\alpha}\right)^k) - \exp(-(\beta/\bar{\alpha})^k)}{1 - \exp(-(\beta/\bar{\alpha})^k)}, \tag{19}$$

where $d_j = \left\| \mathbf{x}_j^i - \mathbf{x}_1^i \right\|$, $\bar{\alpha} = \beta/\omega$ and $\beta = \gamma d_{\max}$, where $d_{\max} = \max\left\{ d_j; \ j = 1, 2, \dots, n_i \right\}$. In order to assign nonzero weights for each point in a local cloud the assumption $\gamma > 1$ is adopted.

4.4. Shape functions

Consider the ith local cloud $\hat{\Omega}_i$ and given function values $\mathbf{w}_i = \left(w_1^i, w_2^i, \dots, w_{n_i}^i \right)^T$ at corresponding points $\mathbf{x}_j^i$. Substituting $\boldsymbol{\alpha}_i = \mathbf{C}_i \mathbf{w}_i$ into (11)

$$\hat{w}_i(\mathbf{x}) = \mathbf{p}^T(\mathbf{x})\boldsymbol{\alpha}_i = \mathbf{p}^T(\mathbf{x})\mathbf{C}_i \mathbf{w}_i = (p_1(\mathbf{x}), p_2(\mathbf{x}), \dots, p_m(\mathbf{x}))\, \mathbf{C}_i \mathbf{w}_i. \tag{20}$$

According [10] the *vector of shape functions* $\boldsymbol{\psi}_i^T(\mathbf{x}) = \left(\psi_1^i(\mathbf{x}), \psi_2^i(\mathbf{x}), \dots, \psi_{n_i}^i(\mathbf{x}) \right)$ is defined as follows

$$\boldsymbol{\psi}_i^T(\mathbf{x}) := \mathbf{p}^T(\mathbf{x})\mathbf{C}_i. \tag{21}$$

Function $\hat{w}_i(\mathbf{x})$ can be rewritten using linear combination of shape functions as

$$\hat{w}_i(\mathbf{x}) = \sum_{j=1}^{n_i} \psi_j^i(\mathbf{x}) w_j^i = \boldsymbol{\psi}_i^T(\mathbf{x})\mathbf{w}_i. \tag{22}$$

Shape function $\psi_j^i(\mathbf{x})$ corresponds to the jth point in the local cloud $\hat{\Omega}_i$.

Taking advantage of the notation (21) and the multi-index notation $\boldsymbol{a} = (a_1, a_2, \dots, a_d)$, the derivatives of shape functions can be expressed in the following way[2]

$$\partial^{\boldsymbol{a}} \boldsymbol{\psi}_i^T(\mathbf{x}) = \left(\partial^{\boldsymbol{a}} p_1(\mathbf{x}), \partial^{\boldsymbol{a}} p_2(\mathbf{x}), \dots, \partial^{\boldsymbol{a}} p_m(\mathbf{x}) \right) \mathbf{C}_i. \tag{23}$$

---

[2] Multi-index derivative notation of a function $f : \mathbb{R}^d \to \mathbb{R}$; $\partial^{\boldsymbol{a}} f(\mathbf{x}) := \frac{\partial^{|\boldsymbol{a}|} f(\mathbf{x})}{\partial x_1^{a_1} \dots \partial x_d^{a_d}}$, $|\boldsymbol{a}| := \sum_{k=1}^d a_k$.

Shape functions fulfil the partition of unity property, cf. [10,19],

$$\sum_{j=1}^{n_i} \psi_j^i(\mathbf{x}) = 1 \tag{24}$$

which will be applied in the derivation of a stable numerical scheme in Section 4.6.

4.5. Stability of WLSQ approximation in the context of FPM

The stability and accuracy of WLSQ approximation are essential for the FPM, cf. [18]. Using the shape functions (21) the stability of the approximation (22) and its derivatives $\partial^a \hat{w}_i(\mathbf{x})$ can be measured by the condition number $\kappa(\mathbf{A}_i)$ of the matrix $\mathbf{A}_i$. The condition number (or the stability of approximation) is mainly influenced by the geometrical distribution of points in a local cloud and by the weighting function. An example of ill-conditioned (or even singular) matrix $\mathbf{A}_i$ can be obtained using the local cloud where all points lie on a single line or if two points lie very close to each other.

Therefore, each local cloud is constructed in accord with the following WLSQ procedure. The condition number of $\mathbf{A}_i$, the largest absolute entry in $\mathbf{A}_i^{-1}$ and the accuracy of approximation for known functions and their derivatives is tested for each local cloud, cf. [25]. In this work the conditions $\kappa(\mathbf{A}_i) < 10^{12}$ and $\|\mathbf{A}_i^{-1}\|_{\max} < 10^{10}$ have been adopted.

The construction of each local cloud has been initiated using the search of all neighbouring points within given radius to the star point in order to fulfil the requirement of minimal number of points $n_i \geq m$, cf. Section 4.2. The local cloud has been accepted if all tests described above were successful. If not, then next neighbouring point has been added to the local cloud and tests have been repeated.

4.6. FPM for 2D linearized Euler equations

Consider a domain $\Omega \subset \mathbb{R}^d$ ($d = 2$) with the boundary $\Gamma = \partial\Omega$. Then the initial-value boundary problem (IVBP) for 2D LEE is given as follows

$$\text{(PDEs)} \quad \frac{\partial \mathbf{w}}{\partial t} + \sum_{k=1}^{d} \frac{\partial \mathbf{F}_k(\mathbf{w})}{\partial x_k} = \mathbf{0}, \quad \mathbf{x} \in \Omega,\ t > 0, \tag{25}$$

$$\text{(IC)} \quad \mathbf{w}(\mathbf{x}, 0) = \mathbf{w}_{\text{in}}(\mathbf{x}), \quad \mathbf{x} \in \Omega, \tag{26}$$

$$\text{(BC)} \quad \mathbf{w}(\mathbf{x}, t) = \mathbf{w}_{\overline{\Gamma}}(\mathbf{x}, t), \quad \mathbf{x} \in \overline{\Gamma},\ t > 0, \tag{27}$$

where $\mathbf{w} = (\rho', u', v', p')^T$ now denotes the fluctuating variables (according Eq. (6)) and the flux $\mathbf{F}_k(\mathbf{w}) = \mathbb{A}_k(\mathbf{w}_0)\mathbf{w}$. We assume a uniform underlying flow, i.e. $\mathbf{w}_0(\mathbf{x}) = \mathbf{w}_0 \Rightarrow \mathbf{H} = \mathbf{0}$. Moreover, $\overline{\Gamma} \subseteq \Gamma$ denotes the part of the boundary, where the BC is prescribed.

Let the global cloud $\hat{\Omega} = \{\mathbf{x}_i\}_{i=1}^{n}$ is given. For each point $\mathbf{x}_i \in \hat{\Omega}$ the corresponding local cloud $\hat{\Omega}_i$ consisting of n_i points is known. Next, for each point $\mathbf{x}_i \in \hat{\Omega}$ the local approximation $\hat{\mathbf{w}}^i(\mathbf{x}, t)$ of $\mathbf{w}(\mathbf{x}, t)$ can be constructed at the domain Ω_i as follows

$$\hat{\mathbf{w}}^i(\mathbf{x}, t) = \sum_{j=1}^{n_i} \psi_j^i(\mathbf{x})\mathbf{w}_j^i(t), \quad i = 1, \ldots, n. \tag{28}$$

Similarly, the flux $\mathbf{F}_k(\mathbf{x}, t) := \mathbf{F}_k(\mathbf{w}(\mathbf{x}, t))$, $k = 1, 2$ can be locally approximated at domains Ω_i as follows

$$\hat{\mathbf{F}}_{k,i}(\mathbf{x}, t) = \sum_{j=1}^{n_i} \psi_j^i(\mathbf{x})\mathbf{F}_k(\mathbf{w}_j^i(t)), \quad i = 1, \ldots, n. \tag{29}$$

In order to obtain the semi-discrete form of governing equation, the collocation method is adopted, i.e. the expression

$$\left[\frac{\partial \hat{\mathbf{w}}^i(\mathbf{x}, t)}{\partial t} + \sum_{k=1}^{d} \frac{\partial \hat{\mathbf{F}}_{k,i}(\mathbf{x}, t)}{\partial x_k}\right]_{\mathbf{x}=\mathbf{x}_i} = 0 \tag{30}$$

has to be satisfied or more precisely

$$\sum_{j=1}^{n_i} \psi_j^i(\mathbf{x}_i) \frac{d\mathbf{w}_j^i(t)}{dt} = -\sum_{k=1}^{d} \sum_{j=1}^{n_i} \frac{\partial \psi_j^i}{\partial x_k}(\mathbf{x}_i) \mathbf{F}_k(\mathbf{w}_j^i(t)) \tag{31}$$

for $\mathbf{x}_i \notin \overline{\Gamma}$. From (27) we have $\mathbf{w}_j^i(t) = \mathbf{w}_{\overline{\Gamma}}(\mathbf{x}_j^i, t)$ for $\mathbf{x}_i \in \overline{\Gamma}$ and from (26) we obtain $\mathbf{w}_j^i(0) = \mathbf{w}_{in}(\mathbf{x}_j^i)$. Next necessary step is the stabilization of the scheme (31). It is based on scaling the stencil of points (Fig. 2) to one half, cf. [19,26–29] and utilizing the partition of unity property (24).
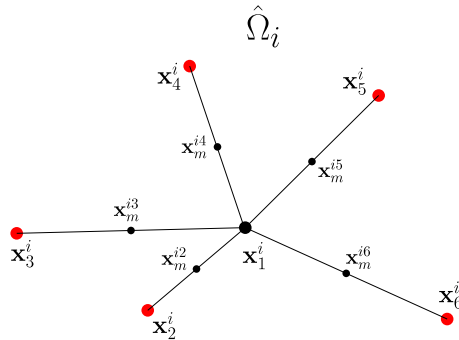
Fig. 2. Midpoints $\mathbf{x}_m^{ij}$ for the local cloud $\hat{\Omega}_i = \left\{\mathbf{x}_1^i, \mathbf{x}_2^i, \ldots, \mathbf{x}_6^i\right\}$.

Collocation of governing equations and above mentioned stabilization of the scheme results in the initial-value problem (IVP) for $\mathbf{w}_j^i(t) \approx \mathbf{w}(\mathbf{x}_j^i, t)$,

$$\text{(ODEs)} \quad \sum_{j=1}^{n_i} \psi_j^i(\mathbf{x}_i) \frac{d\mathbf{w}_j^i(t)}{dt} = -2 \sum_{k=1}^{d} \sum_{j=2}^{n_i} \frac{\partial \psi_j^i}{\partial x_k}(\mathbf{x}_i) \left(\mathbf{F}_k^{ij+1/2} - \mathbf{F}_k^{i1}\right), \tag{32}$$

$$\text{(IC)} \quad \mathbf{w}_j^i(0) = \mathbf{w}_{in}(\mathbf{x}_j^i), \tag{33}$$

where $\mathbf{F}_k^{i1} := \mathbf{F}_k(\mathbf{w}_1^i(t))$ and $\mathbf{F}_k^{ij+1/2}$ is *a priory* unknown flux, cf. Section 4.7. The resulting IVP (32), (33) has to be solved using a high order method in time, cf. Section 4.9.

4.7. Midpoint flux

The flux $\mathbf{F}^{ij+1/2}$ or its components in the kth direction $\mathbf{F}_k^{ij+1/2}$, $k = 1, \ldots, d$, are *a priory* unknown and have to be computed with respect to the governing equations. If the hyperbolic system is linear, then the required flux can be obtained exactly by solving the Riemann problem. Due to the linearity of LEE, we will pay attention to the derivation of exact solution to the Riemann problem following the ideas of Godunov, cf. [30,31].

Consider ith local cloud $\hat{\Omega}_i$ with corresponding star point $\mathbf{x}_1^i$ and one particular neighbouring point $\mathbf{x}_j^i \in \hat{\Omega}_i$. Let us denote the vector connecting both points by $\mathbf{l}_{ij}$ and the corresponding unit vector by $\mathbf{n}_{ij} = (n_1^{ij}, n_2^{ij}, \ldots, n_d^{ij})$, i.e.

$$\mathbf{n}_{ij} = \frac{\mathbf{l}_{ij}}{\|\mathbf{l}_{ij}\|}, \quad \text{where } \mathbf{l}_{ij} = \mathbf{x}_j^i - \mathbf{x}_1^i. \tag{34}$$

The flux $\mathbf{F}^{ij+1/2}$ represents the flow from the star point $\mathbf{x}_1^i$ to its neighbour $\mathbf{x}_j^i$, so it can be obtained as an approximation of the directional flux

$$\tilde{\mathbf{F}}(\mathbf{w}) = \sum_{k=1}^{d} n_k^{ij} \mathbf{F}_k(\mathbf{w}) \tag{35}$$

at the point $\mathbf{x}_m^{ij} := \frac{1}{2}(\mathbf{x}_1^i + \mathbf{x}_j^i)$, cf. Fig. 3.
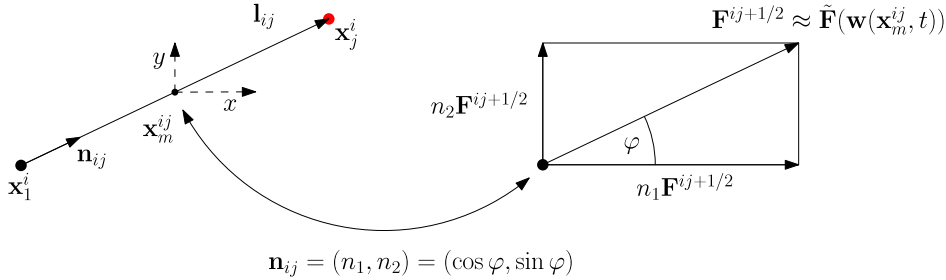

$$\mathbf{n}_{ij} = (n_1, n_2) = (\cos\varphi, \sin\varphi)$$

Fig. 3. Particular 2D flux $\mathbf{F}^{ij+1/2}$ for star point $\mathbf{x}_1^i$ and its neighbour $\mathbf{x}_j^i \in \hat{\Omega}_i$.

Proposition 4.2 (*Godunov Flux*). *Flux components* $\mathbf{F}_k^{ij+1/2}$ *can be obtained as follows*

$$\mathbf{F}_k^{ij+1/2} = \mathbf{F}_G(\mathbf{w}_m^-, \mathbf{w}_m^+) n_k^{ij}, \tag{36}$$

where

$$\mathbf{F}_G(\mathbf{w}_m^-, \mathbf{w}_m^+) = \frac{1}{2}\left[\tilde{\mathbf{F}}(\mathbf{w}_m^-) + \tilde{\mathbf{F}}(\mathbf{w}_m^+)\right] - \frac{1}{2}|\mathbb{A}|\left(\mathbf{w}_m^+ - \mathbf{w}_m^-\right) \tag{37}$$

is the Godunov flux, $\mathbf{w}_m^-$ *and* $\mathbf{w}_m^+$ *are approximation of* $\mathbf{w}$ *at* $\mathbf{x}_m^{ij}$ *from left and right on the line segment* $\overline{\mathbf{x}_1^i \mathbf{x}_j^i}$, *respectively. Matrix* $\mathbb{A} = \sum_{k=1}^{d} n_k^{ij} \mathbb{A}_k$ *is the Jacobian matrix of the flux* $\tilde{\mathbf{F}}(\mathbf{w})$. *If* $\mathbb{A} = \mathbb{T}\mathbb{D}\mathbb{T}^{-1}$ *is the eigendecomposition of matrix* $\mathbb{A}$, *then* $|\mathbb{A}| = \mathbb{T}|\mathbb{D}|\mathbb{T}^{-1}$, *where* $|\mathbb{D}|$ *is the diagonal matrix whose elements are the absolute values of corresponding eigenvalues.*

4.8. Reconstruction of variables

The reconstruction of variables means replacing $\mathbf{w}_m^-$ and $\mathbf{w}_m^+$ in (37) by more accurate approximations. We recommend the reconstruction of variables, cf. [3,5], by means of the Taylor polynomial $\mathcal{T}_\nu(\mathbf{x})$ of degree ν evaluated at midpoint $\mathbf{x}_m^{ij}$, where the derivatives are obtained from local approximations $\hat{\mathbf{w}}^i(\mathbf{x}, t)$, cf. (28).

Consider ith local cloud $\hat{\Omega}_i = \left\{\mathbf{x}_j^i\right\}_{j=1}^{n_i}$ which consists of the star point $\mathbf{x}_1^i$ and its neighbours $\mathbf{x}_j^i$, $j = 2\ldots, n_i$. We will focus on the reconstruction for one pair of points: star point $\mathbf{x}_1^i$ and its neighbour $\mathbf{x}_j^i$ which has its own local cloud $\hat{\Omega}_k = \left\{\mathbf{x}_l^k\right\}_{l=1}^{n_k}$, $\mathbf{x}_1^k = \mathbf{x}_j^i$. Then we can construct $\mathbf{w}_m^-(t), \mathbf{w}_m^+(t)$ as follows

$$\mathbf{w}_m^- = \mathcal{T}_\nu^i(\mathbf{x}_m^{ij}) = \sum_{|\boldsymbol{a}| \leq \nu} \frac{(\mathbf{x}_m^{ij} - \mathbf{x}_1^i)^{\boldsymbol{a}}}{\boldsymbol{a}!} \frac{\partial^{|\boldsymbol{a}|}}{\partial \mathbf{x}^{\boldsymbol{a}}} \hat{\mathbf{w}}^i(\mathbf{x}_1^i, t), \tag{38}$$

where $\boldsymbol{a} = (a_1, a_2, \ldots, a_d)$ is the multi-index. Value $\mathbf{w}_m^- \approx \mathbf{w}^i(\mathbf{x}_m^{ij}, t)$ using the local cloud $\hat{\Omega}_i$.

Similarly,

$$\mathbf{w}_m^+ = \mathcal{T}_\nu^k(\mathbf{x}_m^{ij}) = \sum_{|\boldsymbol{a}| \leq \nu} \frac{(\mathbf{x}_m^{ij} - \mathbf{x}_1^k)^{\boldsymbol{a}}}{\boldsymbol{a}!} \frac{\partial^{|\boldsymbol{a}|}}{\partial \mathbf{x}^{\boldsymbol{a}}} \hat{\mathbf{w}}^k(\mathbf{x}_1^k, t). \tag{39}$$

Value $\mathbf{w}_m^+ \approx \mathbf{w}^k(\mathbf{x}_m^{ij}, t)$ using the local cloud $\hat{\Omega}_k$.

Values $\mathbf{w}_m^-$, $\mathbf{w}_m^+$ vary depending on the degree ν of the Taylor polynomial. Of course, the reconstruction is limited by the basis $\mathcal{B}$. If we consider a complete polynomial basis of degree m, then the Taylor polynomial of degree $\nu \leq m$ can be constructed.

Definition 4.2. The reconstruction of variables $\mathbf{w}_m^-$, $\mathbf{w}_m^+$ is said a ν-*order reconstruction* if the values $\mathbf{w}_m^-$, $\mathbf{w}_m^+$ are obtained using the Taylor polynomial of degree ν.

The 0-order reconstruction reads as

$$\mathbf{w}_m^- = \mathcal{T}_0^i(\mathbf{x}_m^{ij}) = \hat{\mathbf{w}}^i(\mathbf{x}_1^i, t), \qquad \mathbf{w}_m^+ = \mathcal{T}_0^k(\mathbf{x}_m^{ij}) = \hat{\mathbf{w}}^k(\mathbf{x}_1^k, t), \tag{40}$$

which means that the simplest reconstruction coincides with the evaluation of the local approximations $\hat{\mathbf{w}}^i(\mathbf{x}, t)$ at their star points.

Following example shows local approximations $\hat{w}^i(x, t)$, $\hat{w}^k(x, t)$ and Taylor polynomials $\mathcal{T}_\nu^i(x)$, $\mathcal{T}_\nu^k(x)$ which are constructed on 1D domains Ω_i and Ω_k. Both local clouds $\hat{\Omega}_i$ and $\hat{\Omega}_k$ consist of five points (see Figs. 4 and 5).

4.9. Time discretization

The initial problem (32), (33) should be solved with high-order method as well. Therefore, we use the 5-stage LDDRK, cf. [32]. The IVP in form

$$\dot{\mathbf{y}}(t) = \mathbf{f}(\mathbf{y}(t)), \quad t > 0, \tag{41}$$

$$\mathbf{y}(0) = \mathbf{y}_0, \tag{42}$$
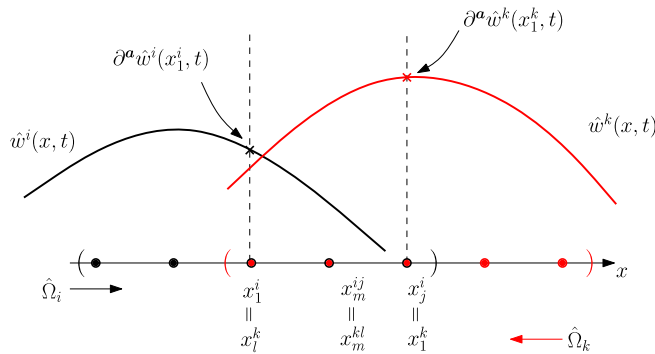
Fig. 4. Local approximations $\hat{w}^i(\mathbf{x}_m^{ij}, t)$, $\hat{w}^k(\mathbf{x}_m^{kl}, t)$ on domains Ω_i, Ω_k, respectively.
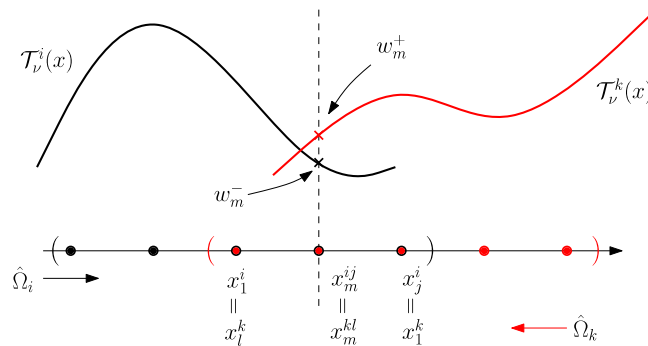
Fig. 5. Taylor polynomials $\mathcal{T}_\nu^i(x)$, $\mathcal{T}_\nu^k(x)$ corresponding to domains Ω_i, Ω_k.

we integrate in time using the time discretization $0 < t_0 < \cdots < t_s = T$. For updating the solution from $\mathbf{y}_n$ to $\mathbf{y}_{n+1}$ the above mentioned method reads as

$$\mathbf{k}_1 = \mathbf{f}(\mathbf{y}_n) \tag{43}$$

$$\mathbf{k}_j = \Delta t \mathbf{f}(\mathbf{y}_n + a_j \mathbf{k}_{j-1}), \quad j = 2, \ldots, 5 \tag{44}$$

$$\mathbf{y}_{n+1} = \mathbf{y}_n + \mathbf{k}_5. \tag{45}$$

The coefficients a_j are listed in Table 1. For uniform distribution of points in the domain the time step Δt is limited by the spatial step h and the mean flow properties as $\Delta t \leq h/(1 + M_0)$, cf. [21].

Table 1
Coefficients for low storage implementation, cf. [32], p. 182, 185.

a_2	a_3	a_4	a_5
0.19771897	0.23717924	0.33311600	0.5

5. Simulation

5.1. 2D acoustic pulse problem

The 2D acoustic pulse problem is the initial-value problem given by the 2D LEE (6) with $\mathbf{H} = \mathbf{0}$ and the initial condition corresponding to the Gaussian acoustic, vorticity and entropy pulse.[3] This problem was proposed by Tam and Webb in [2].

Consider IVP given by

$$(\text{PDEs}) \quad \frac{\partial \mathbf{w}'}{\partial t} + \mathbb{A}_1(\mathbf{w}_0) \frac{\partial \mathbf{w}'}{\partial x} + \mathbb{A}_2(\mathbf{w}_0) \frac{\partial \mathbf{w}'}{\partial y} = \mathbf{0}, \quad (x, y) \in \mathbb{R}^2, \ t > 0, \tag{46}$$

$$(\text{IC}) \quad \mathbf{w}'(x, y, 0) = \mathbf{w}'_{\text{in}}(x, y), \quad (x, y) \in \mathbb{R}^2. \tag{47}$$

The initial condition is prescribed as the superposition of the acoustic and vorticity pulse, both located at point $(x_a, y_a) \in \mathbb{R}^2$ and the entropy pulse located at point $(x_e, y_e) \in \mathbb{R}^2$. Written in compact form, the IC reads as

$$\mathbf{w}'_{\text{in}}(x, y) = \begin{pmatrix} \varepsilon_1 \exp(-\kappa_1 r_a^2) + \varepsilon_2 \exp(-\kappa_2 r_e^2) \\ \varepsilon_3 (y - y_a) \exp(-\kappa_3 r_a^2) \\ -\varepsilon_3 (x - x_a) \exp(-\kappa_3 r_a^2) \\ \varepsilon_1 \exp(-\kappa_1 r_a^2) \end{pmatrix}, \tag{48}$$

where the radius $r_a = \sqrt{(x - x_a)^2 + (y - y_a)^2}$, $r_e = \sqrt{(x - x_e)^2 + (y - y_e)^2}$ and parameters $\kappa_j = (\ln 2)/b_j^2$. The amplitude and the half-width of the acoustic, vorticity and entropy initial pulse are determined by ε_j and b_j, respectively.

We assume the subsonic uniform mean flow in x-direction, i.e. the vector $\mathbf{w}_0 = (\rho_0, u_0, v_0, p_0)^T$ is prescribed as follows

$$\rho_0 = 1, \qquad u_0 = 0.5, \qquad v_0 = 0, \qquad p_0 = \frac{\rho_0}{\gamma} = \frac{5}{7}. \tag{49}$$

---

[3] Fourier analysis of the LEE shows that this equation system enables the propagation of three different waves—acoustic, vorticity and entropy wave. We refer the reader to [1] for further detail.

Then the reference speed of sound a_0 and the Mach number M_0 will be also constant and take the values

$$a_0 = \sqrt{\frac{\gamma p_0}{\rho_0}} = 1 \quad \text{and} \quad M_0 = 0.5. \tag{50}$$

5.2. Analytical solution

We utilize the analytical solution to the 2D acoustic pulse problem (46), (47) for convergence study in Section 5.5. The rigorous derivation can be found in [2, Appendix A].

5.3. Numerical solution

The IVP (46), (47) serves as a benchmark problem in order to study the behaviour of the numerical solution, when the interaction between three types of waves is presented. Let us choose a bounded domain $\Omega = (-24, 24) \times (-24, 24)$. We prescribe the centre of initial acoustic and vorticity pulse at point $(x_a, y_a) = (-9, 0)$, while the centre of initial entropy pulse is moved to the point $(x_e, y_e) = (0, 9)$. Parameters of each initial pulse, cf. (48), are summarized in Table 2.

Table 2
Parameters ε_j and b_j used in IC (48).

$\varepsilon_1 = 0.01$	$b_1 = 3$
$\varepsilon_2 = 0.002$	$b_2 = 3$
$\varepsilon_3 = 0.0008$	$b_3 = 3$

The acoustic waves propagate with the speed of sound $a_0 = 1$ in all directions and moreover they are convected with the velocity $u_0 = 0.5$. In order to avoid the interaction with the boundary of Ω, we will compute just to time $T = 10$. Let us describe the spatial and time discretization. Domain Ω and the initial condition is depicted schematically in Fig. 6.
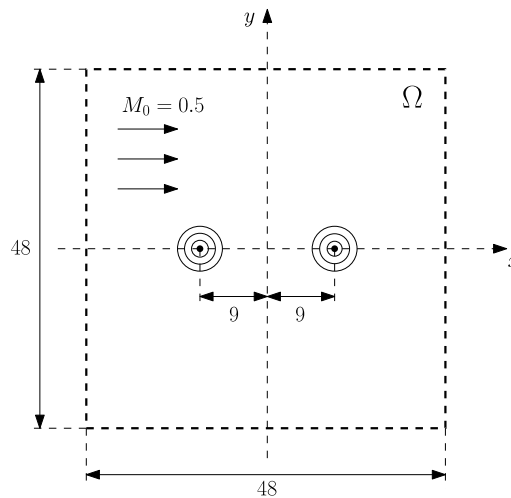
Fig. 6. Bounded domain Ω and the initial condition.

5.4. Spatial and time discretization

Let $h = dx = dy$ denotes the spatial step in x-direction and y-direction. Thus, the uniform discretization of the domain Ω is adopted. We will compute the solution for four spatial steps $h = 1, 0.8, 0.6, 0.4$ and corresponding global clouds will therefore consist of 2401, 3721, 6561, 14 641 points, respectively. The complete polynomial basis $\mathcal{B}$ of degree 3, cf. (15), has been chosen. The basis consists of $m = 10$ functions, i.e. each local cloud $\hat{\Omega}_i$, $i = 1, \dots, n$,

has to contain at least 10 points. Initial search radius $r_i = 3.30h$ is chosen for each point $\mathbf{x}_i \in \hat{\Omega}$, cf. Definition 4.1. Weighting function parameters were chosen as $(\omega, k, \gamma) = (3.1, 2, 1.01)$, cf. Section 4.3. We utilize the 5-stage LDDRK, cf. Section 4.9.

5.5. Convergence study

Table 3 contains the comparison between analytical and numerical solutions for the acoustic density measured by the maximal absolute error $E_{\max}$

$$E_{\max} = \max \left| \left[\rho' \right]_T^i - \rho'(x_i, y_i, T) \right|, \tag{51}$$

where $\left[\rho' \right]_T^i$ is the numerical solution at point $\mathbf{x}_i$ and time T, for different spatial discretizations and ν-order reconstruction. The maximal absolute error in Table 3 was computed only at points $y_i = 0$ and at time $T = 10$.

Table 3
Maximal error using ν-order reconstruction.

$E_{\max}$	2401 p. ($h = 1$)	3721 p. ($h = 0.8$)	6561 p. ($h = 0.6$)	14 641 p. ($h = 0.4$)
$\nu = 0$	8.664×10^{-4}	7.782×10^{-4}	6.745×10^{-4}	5.422×10^{-4}
$\nu = 1$	2.050×10^{-4}	1.064×10^{-4}	4.526×10^{-5}	1.320×10^{-5}
$\nu = 2$	4.698×10^{-5}	3.140×10^{-5}	1.728×10^{-5}	6.231×10^{-6}
$\nu = 3$	3.226×10^{-5}	1.577×10^{-5}	7.117×10^{-6}	1.168×10^{-6}

The logarithm of the error $\ln(E_{\max})$ was depicted over $\ln(h)$ for each ν. We have fitted the line through obtained points for each reconstruction, cf. Fig. 7. The slopes of these fitted lines provide an estimate of FPM order. Namely, for the ν-order reconstruction, $\nu = 0, 1, 2, 3$, the slopes 0.51, 2.99, 2.21, 3.58 have been obtained, respectively.
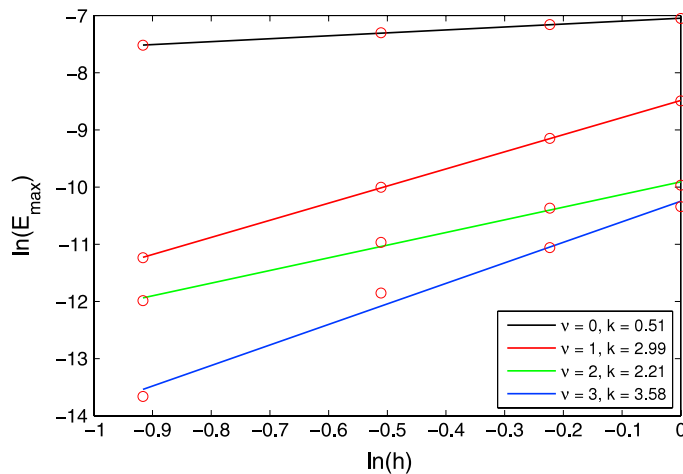
Fig. 7. Convergence study.

The most accurate results were obtained using the 3-order reconstruction. In this case, the FPM reaches almost 4th order (experimental order) of accuracy.

Contours of the solution $\mathbf{w}'(x, y, T)$ of the 2D acoustic pulse problem at time $T = 10$ are depicted in the following 4 figures. The uniform discretization of 14 641 points ($h = 0.4$) and 3-order reconstruction was used (see Figs. 8–11).
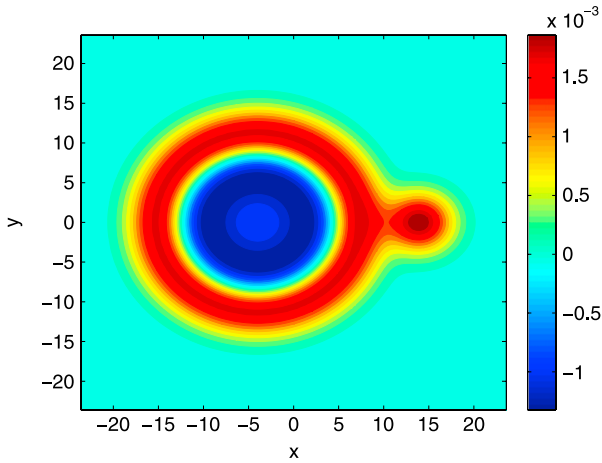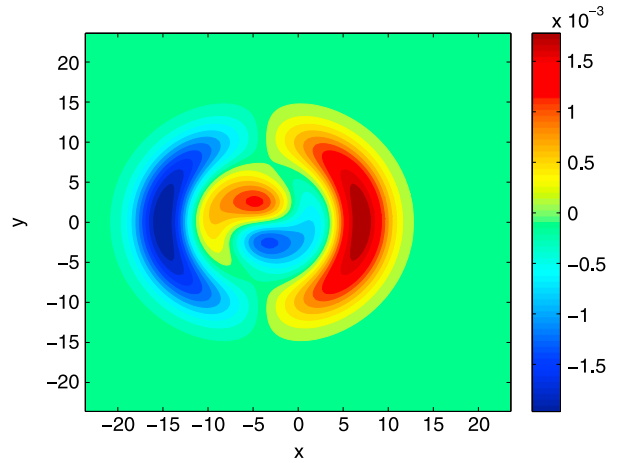
Fig. 8. Density $\rho'(x, y, T)$.

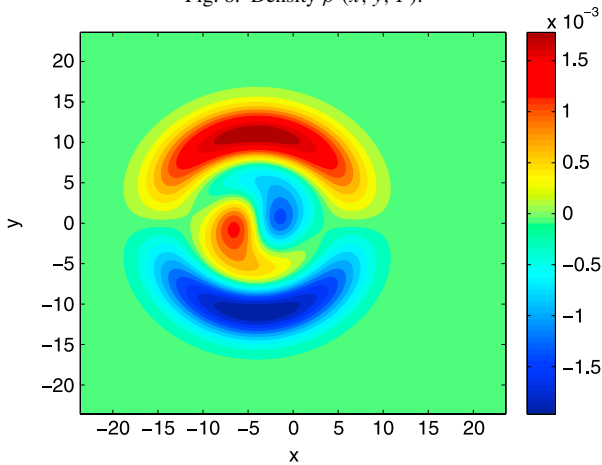Fig. 9. Velocity comp. $u'(x, y, T)$.

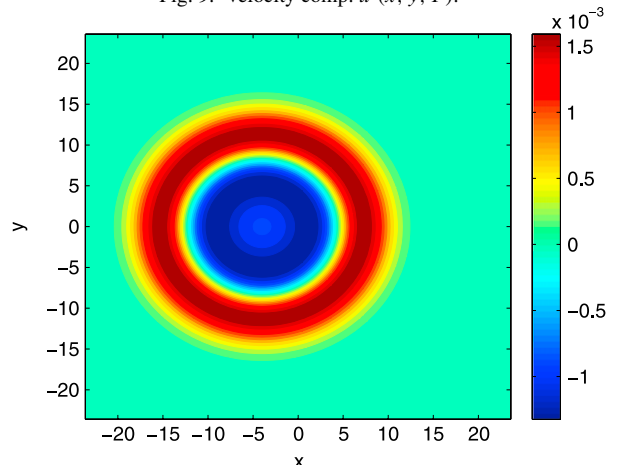Fig. 10. Velocity comp. $v'(x, y, T)$.

Fig. 11. Pressure $\rho'(x, y, T)$.

Figs. 12 and 13 show the acoustic density $\rho'(x, y, T)$, $T = 10$ at points $y = 0$ for the uniform discretization of 2401 points ($h = 1$) and for different reconstruction of variables. The analytical solution is depicted as the solid line.
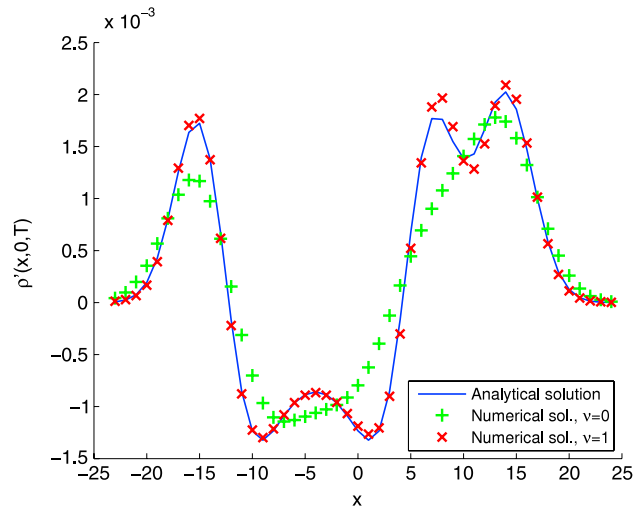

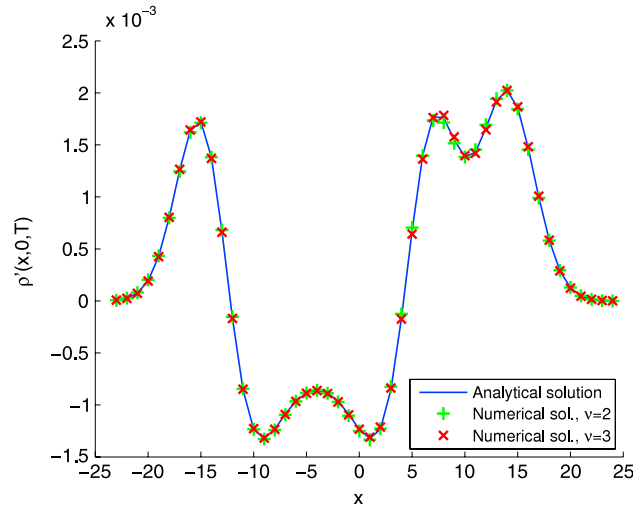Fig. 12. Comparison between zero- and first-order reconstruction.

Fig. 13. Comparison between second- and third-order reconstruction.

5.6. 2D wall bounded acoustic pulse problem

The 2D wall bounded acoustic pulse problem is the IVBP given by 2D LEEs (6) with $\mathbf{H} = \mathbf{0}$ on the rectangular domain Ω together with the Gaussian acoustic initial pulse, given by pressure and density initial distribution

$$
\mathbf{w}'_{\text{in}}(x, y) = \begin{pmatrix} \varepsilon \exp(-\kappa r^2) \\ 0 \\ 0 \\ \varepsilon \exp(-\kappa r^2) \end{pmatrix}.
\tag{52}
$$

Initial acoustic pulse is located at point $(x_a, y_a) = (-50, 0)$, $r = \sqrt{(x - x_a)^2 + (y - y_a)^2}$, with the amplitude $\varepsilon = 1$. Parameter $\kappa = (\ln 2)/b^2$, where the half-width $b = 6$. The geometry and IC are depicted in Fig. 14.
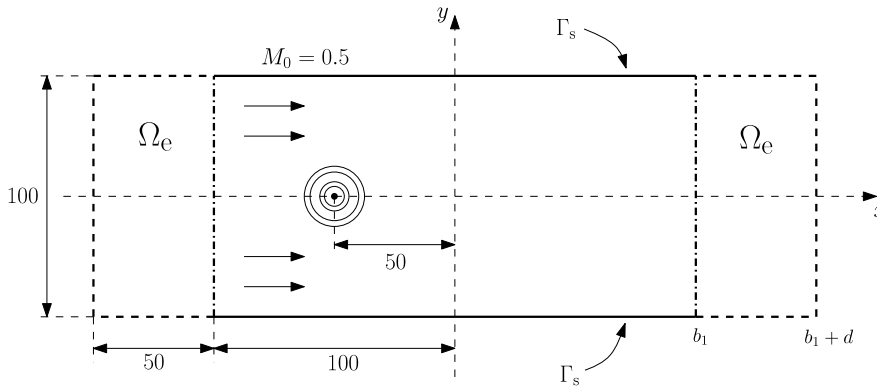
Fig. 14. Rectangular domain Ω, boundaries and initial pulse located at $(-50, 0)$.

5.7. Boundary conditions

The boundary Γ is splitted into two parts. The top and bottom edges of the rectangle Γ_s represent a solid wall, where the slip BC is prescribed. The left and right edges of the rectangle represent an inflow and outflow BC, respectively. These boundaries are modelled using the *absorbing layer* Ω_e, in order to avoid the reflections of travelling waves back

to the domain. Note, the absorbing layer is one possible realization of the so called *non-reflecting boundary condition* (NRBC), cf. [33–35]. Simple absorbing layer can be obtained by the modification of a hyperbolic equation system (25) as follows

$$\frac{\partial \mathbf{w}}{\partial t} + \sum_{k=1}^{d} \frac{\partial \mathbf{F}_k(\mathbf{w})}{\partial x_k} = \sigma(\mathbf{x})(\mathbf{w}_{\text{ref}} - \mathbf{w}), \quad \mathbf{x} \in \Omega_e, \ t > 0, \tag{53}$$

where the function $\sigma : \mathbb{R}^d \to \mathbb{R}$ determines the intensity of damping and $\mathbf{w}_{\text{ref}}$ denotes some reference state ($\mathbf{w}_{\text{ref}} = \mathbf{0}$ for linear systems, cf. [33]). The size of the absorbing layer and the function σ need to be specified for each problem individually.

The intensity of damping given by the damping function $\sigma(x, y)$ should vary smoothly in order to avoid some possible instabilities of a numerical method. One recommended damping function $\sigma(x, y)$ for the 2D rectangular absorbing layers, cf. [33], is given as follows

$$\sigma(x, y) = \begin{cases} 0, & (x, y) \in \Omega \\ \dfrac{\sigma_0}{2}\left(1 + \cos\dfrac{\pi(x - b_1 - d)}{d}\right), & (x, y) \in \Omega_e. \end{cases} \tag{54}$$

Profile of the damping function $\sigma(x, y)$ for the right sponge layer is depicted in Fig. 15.
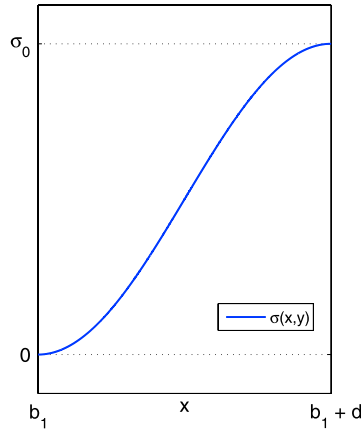
Fig. 15. Damping function $\sigma(x, y)$ profile.

Absorbing effect of the layer Ω_e increases with the damping function $\sigma(x, y)$ given in (53) with the coefficient $\sigma_0 = 0.0625$ and the width of the absorbing layer $d = 50$.

5.8. Numerical solution

The 2D wall bounded pulse problem represents an ideal example for validation of different BC used in CAA, cf. [4]. Perfect reflections should be obtained by slip BC where the solid wall is presented. On the other hand, spurious reflections at inflow and outflow BC should be suppressed as much as possible.
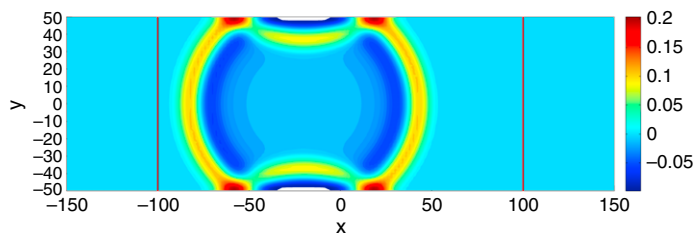

Fig. 16. Pressure contours $p'(x, y, t)$ at time $t \approx 60$.

5.9. Spatial and time discretization

The spatial discretization was chosen as uniform with the spatial step $h = dx = dy = 2$. Thus, the global cloud $\hat{\Omega}$ consists of 7701 points. The basis $\mathcal{B}$, search radius r_i, weighting function parameters $(\omega, k, \gamma) = (3.1, 2, 1.01)$ and time step were chosen identically as for the 2D acoustic pulse problem, cf. spatial and time discretization 5.4. The most accurate 3-order reconstruction for basis $\mathcal{B}$ was utilized, i.e. $\nu = 3$, cf. Section 4.8.
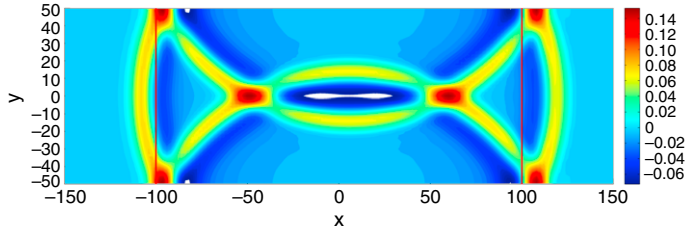
Fig. 17. Pressure contours $p'(x, y, t)$ at time $t \approx 110$.
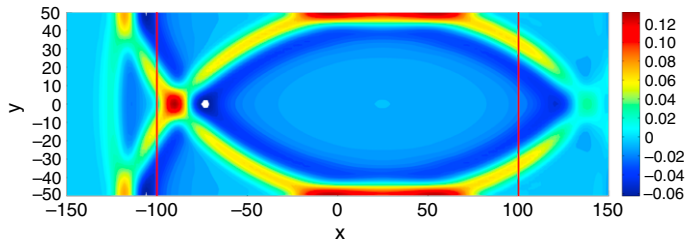
Fig. 18. Pressure contours $p'(x, y, t)$ at time $t \approx 150$.

Pressure contours $p'(x, y, t)$ at times $t = 60, 110, 150, 200, 267$ are depicted in Figs. 16–20.
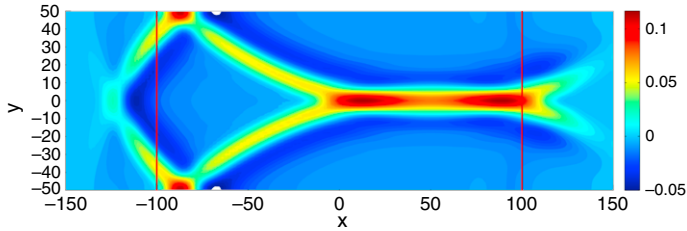
Fig. 19. Pressure contours $p'(x, y, t)$ at time $t \approx 200$.

The non-reflecting boundary condition imposed using the sponge layer Ω_e suppress most incoming waves, but not all indeed. We can observe some spurious waves in Figs. 19 and 20 propagating with the speed of sound a_0 back inside the domain and spoil the solution.
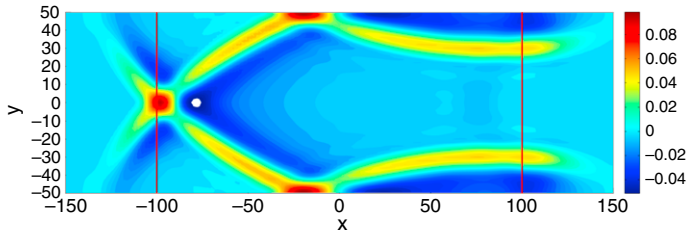

Fig. 20. Pressure contours $p'(x, y, t)$ at time $t \approx 267$.

5.10. 2D acoustic pulse problem on circular domain

Another example aims to demonstrate the ability of the FPM to solve the 2D propagation problem on unstructured point distribution and curved geometry. The IVBP is given by 2D LEEs (6) with $\mathbf{H} = \mathbf{0}$ on circular domain Ω together with the Gaussian acoustic initial pulse, cf. (52), located at point $(x_a, y_a) = (-16, 0)$ with amplitude $\varepsilon = 1$ and half-width $b = 3$. The geometry and IC are depicted in Fig. 21.
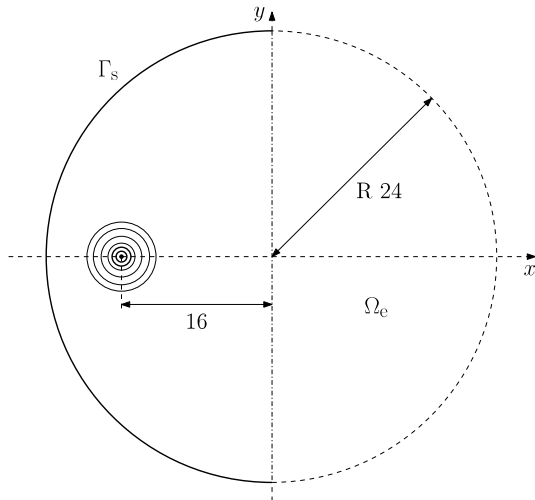

Fig. 21. Circular domain Ω, boundaries and initial pulse located at $(-16, 0)$.
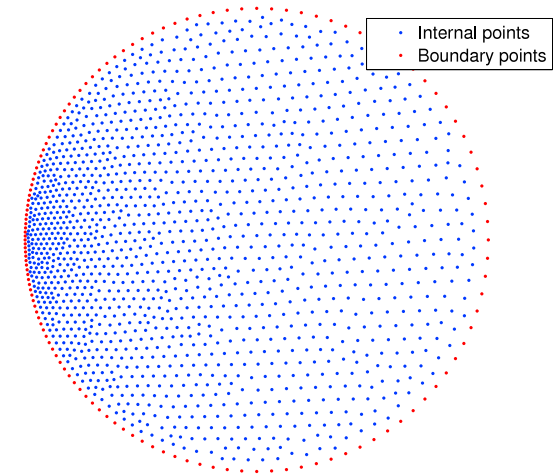
Fig. 22. The point distribution in domain Ω.

We assume the quiescent medium, so the velocity $\mathbf{u}_0 = (u_0, v_0)^T$ of underlying flow, cf. (49), is the zero vector. The slip BC is prescribed on Γ_S. The right hemisphere Ω_e represents an absorbing layer given by the damping function (54) with $b_1 = 0$, $d = 24$ and $\sigma_0 = 1$.

5.11. Spatial and time discretization

The spatial discretization of the domain Ω has been constructed as inhomogeneous with 1553 points refined towards the boundary Γ_S, cf. Fig. 22. The basis (14) has been selected with the first order reconstruction. Search radius r_i has been adjusted in order to initiate each local cloud with 12 points. The weighting function parameters $(\omega, k, \gamma) = (3.1, 2, 1.01)$. The time step has been set to 0.05.
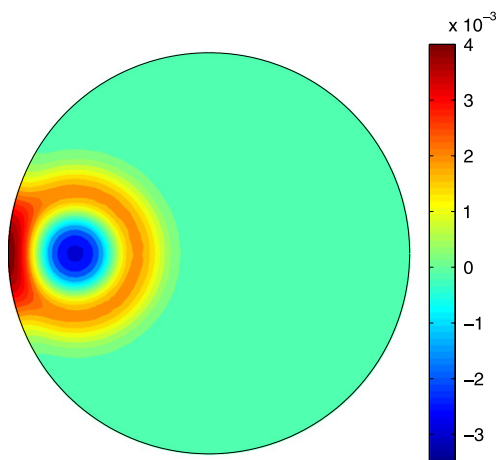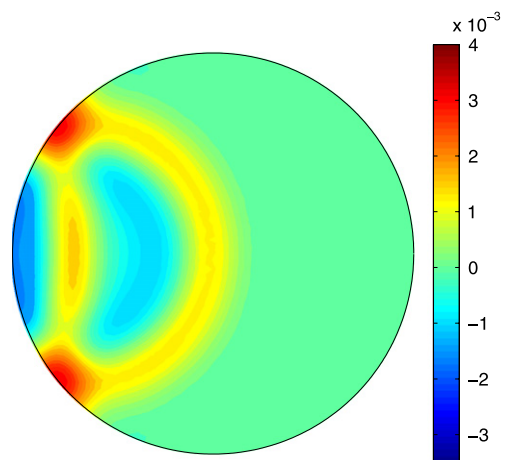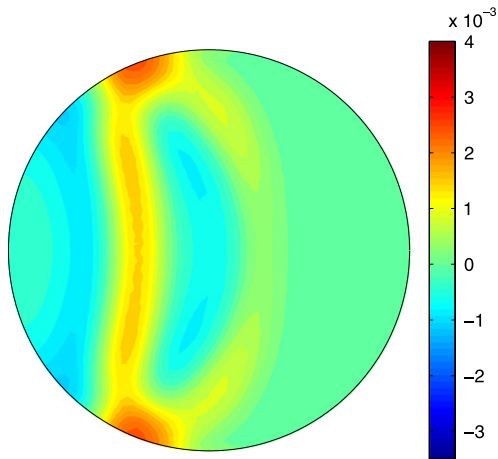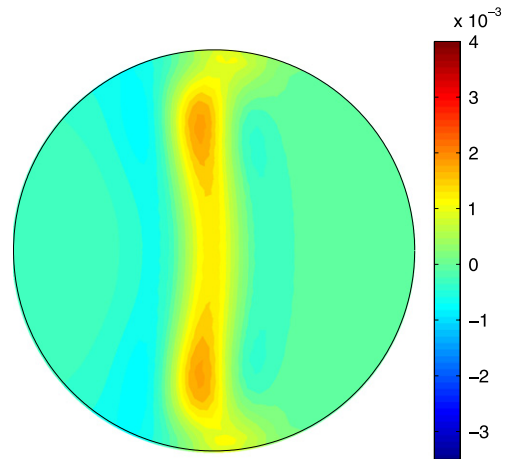

Fig. 23. Pressure contours at time $t = 6$.

Fig. 24. Pressure contours at time $t = 14$.

Pressure contours $p'(x, y, t)$ at times $t = 6, 14, 22, 30$ are depicted in Figs. 23–26.

Fig. 25. Pressure contours at time $t = 22$.

Fig. 26. Pressure contours at time $t = 30$.

The highest accuracy is obtained in the refined region (left hemisphere) whereas the waves propagating to the right disappear partly due to the coarsening of the point distribution and the effect of the absorbing layer.

6. Conclusion

The 2D acoustic pulse problem, cf. Section 5.1, has been solved in order to study the accuracy of FPM for different reconstruction of variables involved in the Riemann solver, cf. Sections 4.7 and 4.8. The analytical solution has been utilized for the comparison of obtained results which were used to estimate the order of FPM, cf. Section 5.5. Clearly, for complete polynomial basis of degree 3, the highest accuracy has been obtained using the 3-order reconstruction. Moreover, the 2D wall bounded acoustic pulse problem, cf. Section 5.6, has been solved using high order FPM. The absorbing layer Ω_e determined by the damping function (54) with $\sigma_0 = 0.0625$ shows a partial suppression of reflected waves. It can be concluded that the FPM with improved Riemann solver satisfies necessary requirement for the sound propagation problems in terms of accuracy. The experimental order of FPM for the 2D acoustic pulse problem is almost 4 for 3-order reconstruction. Finally, the robustness of the FPM has been tested on circular geometry with the inhomogeneous point distribution.

Acknowledgement

References

[1] W.D. Roeck, Hybrid methodologies for the computational aeroacoustic analysis of confined, subsonic flows (Ph.D. thesis), Katholieke Universiteit Leuven, 2007.
[2] C.K.W. Tam, J.C. Webb, Dispersion-relation-preserving finite difference schemes for computational acoustics, J. Comput. Phys. 107 (1993) 262–281.
[3] L. Cueto-Felguroso, I. Colominas, High-order finite volume methods and multiresolution reproducing kernels, Arch. Comput. Methods Eng. 15 (2008) 185–228.
[4] X. Nogueira, I. Colominas, L. Cueto-Felguroso, S. Khelladi, F. Navarrina, M. Casteleiro, Resolution of computational aeroacoustics problems on unstructured grids with a higher-order finite volume scheme, J. Comput. Appl. Math. 234 (2009) 2089–2097.
[5] X. Nogueira, S. Khelladi, I. Colominas, L. Cueto-Felguroso, J. París, H. Gómez, High–resolution finite volume methods on unstructured grids for turbulence and aeroacoustics, Arch. Comput. Methods Eng. 18 (2011) 315–340.
[6] M. Roger, T. Colonius, C. Schran, et al., Computational Aeroacoustic, Von Karman Institute, 2006.
[7] A.V. Wolkov, N.B. Petrovskaya, Higher order discontinuous galerkin method for acoustic pulse problem, Comput. Phys. Commun. 181 (2010) 1186–1194.
[8] T.P. Fries, H.G. Matthies, Classification and overview of meshfree methods, Tech. rep., Institut für Wissenschaftliches Rechnen, http://www.digibib.tu-bs.de/?docid=00001418 [Online], cited 26.6.2014 (2008).

[9] G.R. Liu, Mesh Free Methods: Moving beyond the Finite Element Method, CRC Press, 2003.

[10] G.R. Liu, Y.T. Gu, An Introduction to Meshfree Methods and Their Programming, Springer, Berlin, 2005.

[11] K. Li, Q.B. Huang, J.L. Wang, L.G. Lin, An improved localized radial basis function meshless method for computational aeroacoustics, Eng. Anal. Bound. Elem. 35 (2011) 47–55.

[12] S. Wang, S. Li, Q. Huang, K. Li, An improved collocation meshless method based on the variable shaped radial basis function for the solution of the interior acoustic problems, Math. Probl. Eng. 2012 (2012) 20. pages.

[13] P.R.S. Antunes, S.S. Valtchev, A meshfree numerical method for acoustic wave propagation problems in planar domains with corners and cracks, J. Comput. Appl. Math. 234 (2010) 2646–2662.

[14] E. Oñate, S. Idelsohn, O.C. Zienkiewicz, R.L. Taylor, A finite point method in computational mechanics applications to convective transport and fluid flow, Int. J. Numer. Methods Eng. 39 (1996) 3839–3866.

[15] E. Oñate, Derivation of stabilized equations for numerical solution of advective–diffusive transport and fluid flow problems, Comput. Methods Appl. Mech. Eng. 151 (1998) 233–265.

[16] E. Oñate, C. Sacco, S. Idelsohn, Meshless analysis of incompressible flows using the finite point method, in: J. Periaux, P. Joly, O. Pironneau, E. Oñate (Eds.), Innovative Tools for Scientific Computation in Aeronautical Engineering, CIMNE, Barcelona, 2002.

[17] E. Oñate, F. Perazzo, J. Miquel, Advances in the stabilized finite point meted for structural mechanics, in: European Conference on Computational Mechanics, CIMNE, München, 2003.

[18] E. Ortega, E. Oñate, S. Idelsohn, An improved finite point method for tridimensional potential flows, Comp. Mechanics 40 (2007) 949–963.

[19] E. Ortega, E. Oñate, S. Idelsohn, A finite point method for adaptive three-dimensional compressible flow calculations, Internat. J. Numer. Methods Fluids 60 (2009) 937–971.

[20] I. Ali, S. Becker, J. Utzmann, C.D. Munz, Aeroacoustic study of a forward facing step using linearized euler equations, Physica D 237 (2008) 2184–2189.

[21] C. Bailly, D. Juvé, Numerical solution of acoustic propagation problems using linearized euler equations, AIAA J. 38 (1) (2000).

[22] E. Ortega, E. Oñate, S. Idelsohn, An adaptive finite point method for the shallow water equations, Int. J. Numer. Methods Eng. 88 (2011) 180–204.

[23] A. Angulo, L. Perez-Pozo, F. Perazzo, A posteriori error estimator and an adaptive technique in meshless finite points method, Eng. Anal. Bound. Elem. 33 (2009) 1322–1338.

[24] R. Löhner, C. Sacco, E. Oñate, S. Idelsohn, A finite point method for compressible flow, Int. J. Numer. Methods Eng. 53 (2002) 1765–1779.

[25] F. Perazzo, R. Löhner, L. Perez-Pozo, Adaptive methodology for meshless finite point method, Adv. Eng. Softw. 39 (2008) 156–166.

[26] A. Jameson, Analysis and design of numerical schemes for gas dynamics 1 artificial diffusion, upwind biasing, limiters and their effect on accuracy and multigrid convergence, Int. J. Comput. Fluid Dyn. 4 (1995) 171–218.

[27] A. Katz, A. Jameson, Edge-based meshless methods for compressible flow simulations, AIAA J. 699 (2008).

[28] A.J. Katz, Meshless methods for computational fluid dynamics (Ph.D. thesis), Stanford University, 2009.

[29] A. Katz, A. Jameson, Meshless scheme based on alignment constraints, AIAA J. 48 (11) (2010) 2501–2511.

[30] M. Feistauer, Mathematical Methods in Fluid Dynamics, Longman Scientific & Technical, Harlow, 1993.

[31] E.F. Toro, Riemann Solvers and Numerical Methods for Fluid Dynamics, second ed., Springer-Verlag, 1999.

[32] F.Q. Hu, M.Y. Hussainy, J.L. Manthey, Low-dissipation and low-dispersion Runge–Kutta schemes for computational acoustics, J. Comput. Phys. 124 (0052) (1996) 177–191.

[33] T. Colonius, Modeling artificial boundary conditions for compressible flow, Annu. Rev. Fluid Mech. 36 (2004) 315–345.

[34] J. Dea, High-order non-reflecting boundary conditions for the linearized Euler equations (Ph.D. thesis), Naval Postgraduate School Monterey, California, 2008.

[35] A. Mani, On the reflectivity of sponge zones in compressible flow simulations, Annual Research Briefs (2010) 117–133.